INORGANIC CHEMISTRY

FRONTIERS

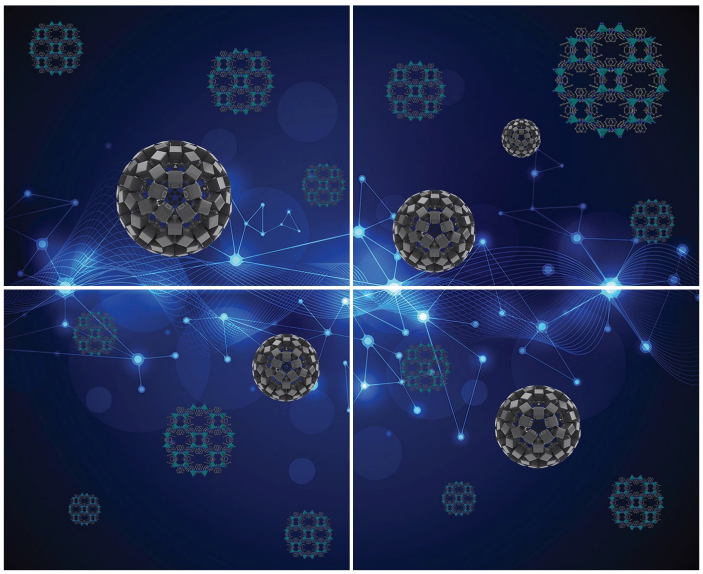

Accepted Manuscript

This article can be cited before page numbers have been issued, to do this please use: S. O. T. Mace, A. S. Goodfellow, B. N. Nguyen, B. S. Grace, M. Bates, M. Halcrow, P. H. Walton and Y. Xu, *Inorg. Chem. Front.*, 2026, DOI: 10.1039/D6QI00844E.

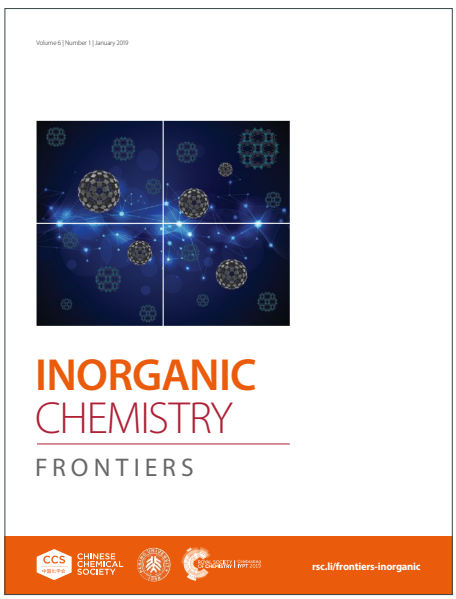

View Article Online
DOI: 10.1039/D6QI00844E

ARTICLE

Prediction of Energies of Spin States for First Row Transition Metal Complexes: DFT *vs* Ligand Field Theory

Received 00th January 20xx,
Accepted 00th January 20xx

DOI: 10.1039/x0xx00000x

Samuel Mace,[a] Benjamin S. Grace,[b] Alister Goodfellow,[a] Martin A. Bates,*[b] Malcolm A. Halcrow,[a] Paul H. Walton,*[b] Yingjian Xu,*[c] and Bao N. Nguyen*[a]

DFT benchmarking on 127 base metal complexes revealed unreliable spin state predictions by B3LYP, PBE0, TPSSh and M06-L functionals, especially when energy gaps between the lowest energy spin states were small. PBE0/def2-TZVP offered the closest optimised geometries to crystal structures but failed to reliably predict spin-crossover (SCO) temperatures (T_{SCO}) for 32 Fe(II) complexes. *Kestrel*, a computational package using ligand field theory, achieved better T_{SCO} predictions and demonstrated high sensitivity to ligand-metal angular arrangement. Application of *Kestrel* to 2 DFT-detected spin-crossover catalytic cycles confirmed agreement on ground-state spins but not SCO in key steps. These findings underscore that DFT-based T_{SCO} predictions based on single complexes should not guide SCO assessments particularly in solid state.

Introduction

Base-metal-catalysed reactions are widely considered more sustainable alternatives to those catalysed by precious metals such as Rh, Ir, Pd and Pt.[1,2] More importantly, base metal catalysts often exhibit different reactivities, particularly those involving single electron transfer, photo- or electrochemical excitation steps, and redox processes, compared to those of precious metals, giving rise to a much wider range of organic transformations.[3–6] Thus, the spin states of the catalytic intermediates and transition states are essential in rational catalyst and ligand design for these reactions. Beyond catalysis, the spin states of base metal complexes are equally critical in molecular switches,[7,8] data storage devices,[9,10] and sensors.[11–13] For transient species such as catalytic intermediates and transition states, a computational approach is the most likely method to probe their spin states and related properties. Current consensus on spin state calculations requires multireference (CASSCF, CASPT2, NEVPT2, and MRCI) methods for reliable results, due to the need for an accurate treatment of distinct electronic configurations and electron correlation.[14–16]

Unfortunately, due to the computational demand, this is impractical when applying to catalytic cycles,[17–19] or in high throughput *in silico* discovery mode.[20] Thus, a wide range of Density Functional Theory (DFT) methods and basis sets have been employed instead, albeit with limited benchmarking between methods to assess their accuracy and reliability. Successful benchmarking studies have been carried out but often for narrow systems, mostly Fe(II) complexes in octahedral geometry, or with few examples,[21,22] instead of with a diverse range of organometallic complexes, whilst requiring some of the most computationally expensive modelling methods, *e.g.* CCSD(T).[23–26] The most diverse benchmarking study on Cr, Mn, Fe and Co complexes was reported by Ruiz *et al*, who concluded that quantitative performance is not accurate enough for spin-crossover (SCO) compounds.[27] A study using semi-empirical method GFN-xTB/GFN2-xTB with a spin-dependent energy term is the only outlier to these general trends of higher cost modelling methods and narrow range of complexes, but its performance was only benchmarked against those of TPSSh-D4/def2-QZVPP.[28] Other researchers have tried to address this gap with machine learning methods with some levels of success, within narrow subsets of electron configurations and geometries.[29–32] In one study, the geometry and metal-ligand bond lengths were used to predict the spin states for 46 Fe(II) SCO complexes.[32] Their performance is again limited by the single-determinantal DFT methods employed to generate the training data for the predictive models.

In this study, we report a benchmarking study of modern DFT methods in predicting the most stable spin states of a set of 127 complexes of Cr(II), Mn(II), Fe(III), Fe(II) and Co(II) with experimentally measured magnetic susceptibility data.[33] The best performing methods were evaluated in calculating the spin-crossover temperature (T_{SCO}) of 32 curated Fe(II) complexes, against experimental data. The results were then compared to those calculated by *Kestrel*,[34] a computational package based on ligand field theory which, in contrast to single-determinantal DFT methods, calculates the energies of all possible metal spin states. The results highlighted the limitations of both approaches, the uncertainties associated

[a] School of Chemistry, University of Leeds, Woodhouse Lane, Leeds, LS2 9JT, United Kingdom.
[b] Department of Chemistry, University of York, Heslington, York, YO10 5DD, United Kingdom.
[c] GoldenKeys High-tech Materials Co., Ltd. Building 3, Guizhou Industrial Investment Technology Industrial Park Gui'an New District, Guizhou Province, 550008, China.

† Footnotes relating to the title and/or authors should appear here.
Supplementary Information available: [details of any supplementary information available should be included here]. See DOI: 10.1039/x0xx00000x

with modelling spin-crossover events, [17,35] and possible solutions.

Methods

Data curation

Metal complexes were searched on Reaxys with the criteria of organometallic complexes having XRD data and magnetic susceptibility data to confirm ground state multiplicity at room temperature. The search was stopped at 150 complexes. The structures were checked manually, and complexes with radical ligands were removed. Oxidation states were assigned to complexes after careful verification using the information in the of relevant papers.

A total of 127 complexes of Cr(II), Mn(II), Fe(III), Fe(II) and Co(II) cations with experimentally determined ground state multiplicities and X-ray crystal structures were curated using Reaxys and CCDC tools.[36] These metals and oxidation states were selected for their possible spin states, experimental data availability and their importance in base metal catalysis and material design. Octahedral and non-octahedral (42% and 58% of the total dataset respectively) structures were included, in contrast to the more geometrically homogeneous dataset previously collected by Cirera, Kepp and Kulik.[25,27,37,38] The composition of this dataset (***base_spin_dataset***) by coordination geometry and multiplicities is summarised in Fig. 1 and Table 1. Some examples of included structures are shown in Table 2.

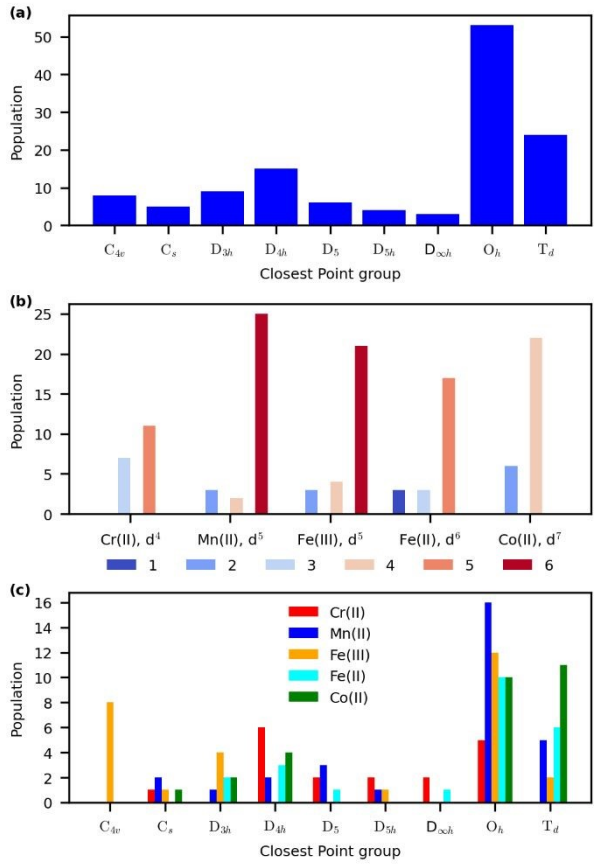

Fig. 1 Analysis of ***base_spin_dataset***, showing the included (a) geometries, (b) metals, their oxidation states and multiplicities (1-6, in different colours), and (c) geometries for different metal centres.

Experimental T_{SCO} values of 32 octahedral Fe(II) complexes were collected from the literature (***T_SCO_dataset***, Fig. 2). The majority of these complexes (26) came from the work of Halcrow *et al.* due to the completeness of their reported data (*e.g.* ΔS and ΔH values).[39]

Table 1 Coordination geometry and approximate point groups

Closest Point Group	Coordination Geometry
C_{4v}	Square base pyramidal
D_{3h}	Trigonal planar or trigonal bipyramidal
D_{4h}	Square planar
C_s	Complex geometries with one mirror plane
D_5	Pentagonal antiprism (*e.g.* Cp^*_2Fe)
D_{5h}	Pentagonal prism (*e.g.* eclipsed Cp_2Fe)
$D_{\infty h}$	Linear
O_h	Octahedral
T_d	Tetrahedral

Table 2 Structural diversity of base metal complexes in ***base_spin_dataset*** and their CCDC identifiers

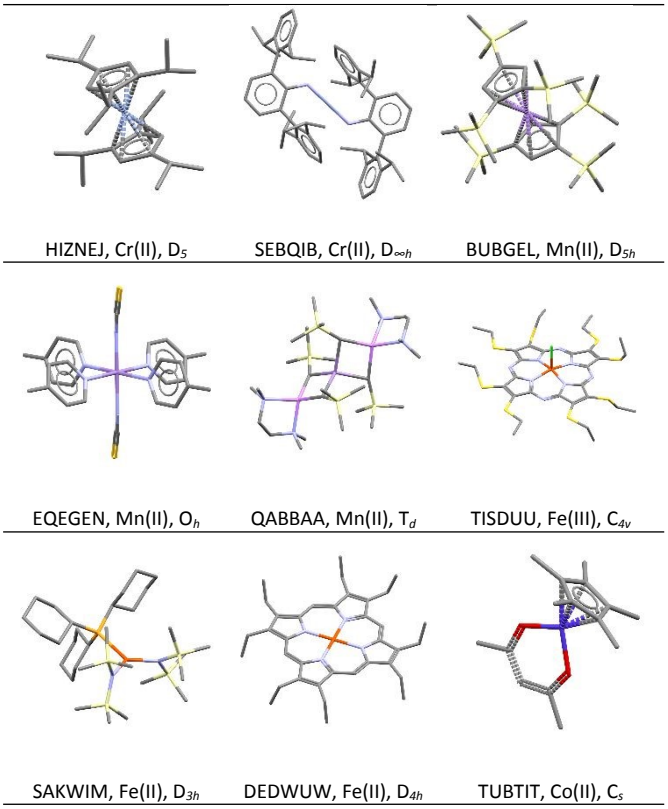

HIZNEJ, Cr(II), D_5	SEBQIB, Cr(II), $D_{\infty h}$	BUBGEL, Mn(II), D_{5h}
EQEGEN, Mn(II), O_h	QABBAA, Mn(II), T_d	TISDUU, Fe(III), C_{4v}
SAKWIM, Fe(II), D_{3h}	DEDWUW, Fe(II), D_{4h}	TUBTIT, Co(II), C_s

DFT calculations

DFT calculations were performed using ORCA 6.0.1, with DEFGRID3 for all 127 complexes in ***base_spin_dataset***.[40] The selected functionals were B3LYP, PBE0, TPSSh and M06-L. The triple-ζ basis set def2-TZVP was used in all cases. These led to good success rates with B3LYP, PBE0, and TPSSh (3 jobs failed each, due the large sizes of the complexes). The M06-L

functionals had a slightly lower success rate, with an additional 2 complexes failed due to persistent imaginary frequencies.
The same four methods and PBE0-D4 were applied to structures in ***T_SCO_dataset***. In addition, r^{2}SCAN/def2-TZVP was included due to its low cost and good results in predicting spin states against TPSSh values.[26] The impact of solvation was assessed for PBE0-D4/def2-TZVP, with SMD solvent model employed for complexes that were measured in nitromethane or acetone. The predicted T_{SCO} values were compared with those predicted in gas phase and experimental values.

Metrics for spin state predictions

The metrics employed to assess the DFT prediction of ground state multiplicity out of three possible multiplicities for ***base_spin_dataset*** are the percentage of predictions with matching DFT calculated lowest energy spin state and experimentally measured spin state (P1-score) and the single point energy gap between the two lowest energy spin states in the gas phase (E1-2, in kcal.mol^{-1}). Cr(II, d^4), Mn(II, d^5), Fe(III, d^5) and Fe(II, d^6) can have multiple spin states, and thus E1-2 avoids the confusion in describing low, middle and high spin states across multiple metal centres.

T_{SCO} predictions

Theoretical T_{SCO} values were calculated for Fe(II) complexes in ***T_SCO_dataset*** using the enthalpy (ΔH) and entropy (ΔS) differences between the high-spin (HS, multiplicity of 5) and low-spin (LS, multiplicity of 1) states:

$$T_{SCO} = \frac{\Delta H_{HS-LS}}{\Delta S_{HS-LS}} \quad (1)$$

The thermodynamic values were calculated at 298 K in the gas phase. Entropies were calculated with modified quasi-harmonic approximation and enthalpies values included thermal vibrational contributions. The calculated T_{SCO} was compared to experimental values. For a subset of PBE0-D4 calculations where the experimental solvent is specified, both gas phase and solvent phase (SMD model) T_{SCO} values were calculated (see ESI, section 3).

Kestrel calculations

Kestrel is a computational package for ligand field calculations. The calculations are performed on monomeric 3d^n (n = 1–9) transition metal complexes in any coordination geometry, employing a full J,m_J set of the Russell-Saunders (RS) states. These RS states are perturbed to first order using three separate effective Hamiltonians (electron-electron repulsion, ligand field and spin-orbit interaction) the sum of which affords an overall effective Hamiltonian. The ligand field Hamiltonian calculates the degree of dynamical electron correlation between the Russell-Saunders components under the effects of the ligand field, through the use of analytical integrals originally developed by Gerloch and Woolley,[41,42] in which it is assumed that spatial overlap between the 3*d* and ligand orbitals is minimal. Diagonalisation of the final configuration interaction matrix, the individual elements of which are calculated using the overall effective Hamiltonian, affords eigenfunctions and eigenvalues for the *d*-configurations of the transition metal complex. These values are used to compute ligand-field transition energies/intensities, paramagnetic susceptibilities and EPR parameters for subsequent correlation with experimental values.[34]

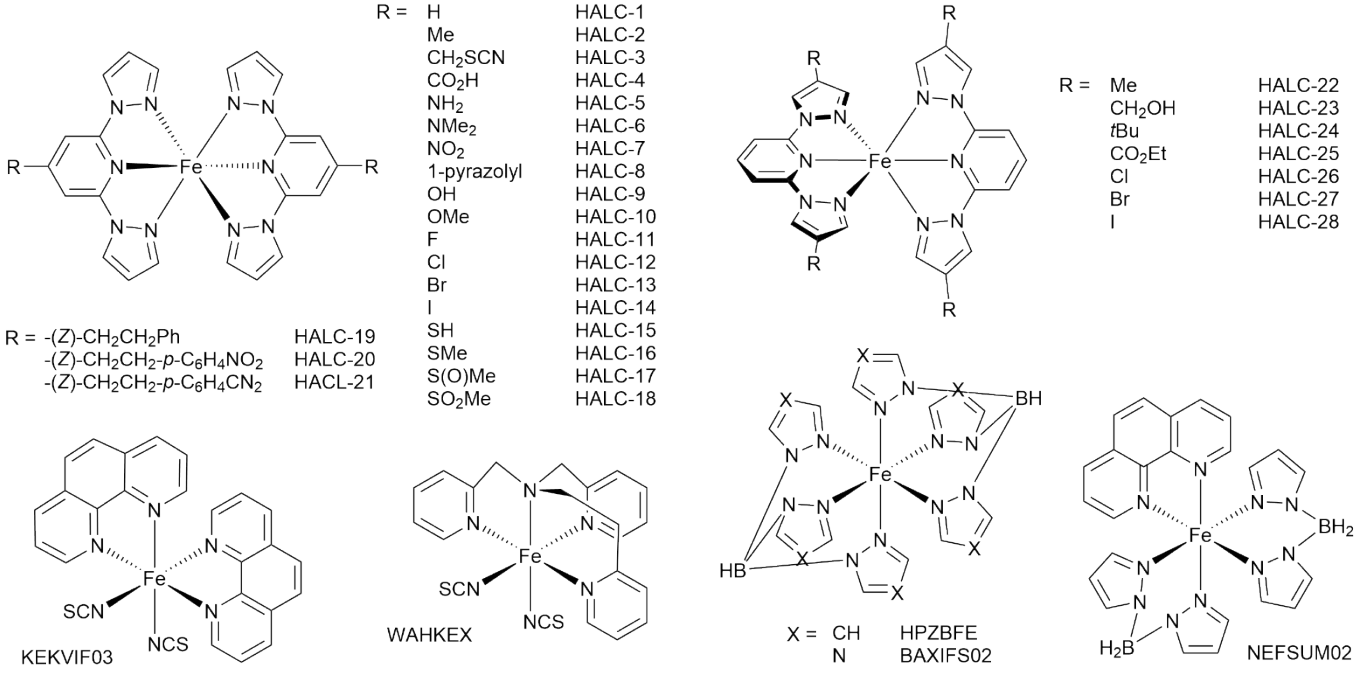

Fig. 2 Chemical structures of complexes in ***T_SCO_dataset***

View Article Online
DOI: 10.1039/D6QI00814B

One key advantage of the "Gerloch method" which *Kestrel* employs is that the overall ligand field Hamiltonian is calculated from the sum of individual σ- and π-bonding properties of each ligand. These individual interactions are quantified using *e-values*, parameters taken from the angular overlap model, which are chemically intuitive. However, it is worth noting that *Kestrel* is not an angular overlap model *per se*, as no covalent overlap is assumed between ligand and metal-based *d*-orbitals.

Since Kestrel only calculates the differences in electronic energies, factors such as the difference in entropies of the low- and high-spin states are not accounted for. For individual complexes, this presents a major contribution to the T_{SCO}, making calculations with Kestrel to calculate the T_{SCO} of single molecules unfeasible,[38,43–46] since the entropic contribution will lead to an 'unchemical' reduction in *e*-values of the high-spin state. However, in this study, Kestrel is used to examine the *differences* in T_{SCO} for a series of related complexes where the entropy contribution to the T_{SCO} is known to be constant (within the error of DFT calculations) across the series. Thus, the entropic factors leading to a reduction in *e*-values apply equally to all of the complexes in this study.

Consequently, the RS-state eigenfunctions and eigenvalues were calculated using *Kestrel* for each of the DFT-determined [*bis*-{*bis*-(X-pyrazolyl)-Y-pyridine}Fe(II, d^6)] (PBE0/def2-TZVP) structures in **T_SCO_dataset**,[39] for which DFT calculation revealed a constant entropy change within an error of ±1 kJ mol^{-1} (Fig.S38) that is smaller the >1-5 kcalmol^{-1} error of DFT methods.[16] Due to Kestrel's multiconfigurational analysis, low-spin (singlet) structures were employed allowing the relative energy of the high-spin state to be calculated. Paramagnetic susceptibility *vs* temperature plots were then simulated within *Kestrel,* with the mid-point of these plots ($T_{1/2}$ = 1.5 cm^3.K.mol^{-1}) giving individual T_{SCO}'s (Fig. 3a) which could be compared to experiment. In the first instance, a plot of calculated *vs* experimental T_{SCO}'s was created, using a fixed set of ligand field parameters for all complexes (Fig. S30/S31). (It is noted that, for R = –NH_2 (HALC-5) and –NMe_2 (HALC-6), experimental T_{SCO}'s are unavailable due to the complexes remaining high-spin over the liquid range of the solvent.) The *e*-parameters and *Racah B, C* values were derived from fitting to the magnetic and spectroscopic data of the unsubstituted Fe(II) HALC-1 complex (R = H).[47,48] The resulting e_σ parameters for pyridine in this analysis are greater than pyrazolyl by ~1000 cm^{-1}, indicating that the pyridine ligands are stronger σ-donors. In addition, the pyridine ligands have negative e_π parameters denoting them as π-acceptors whereas the pyrazolyl ligands have small positive e_π parameters denoting them as weak π-donors (Table 3). Necessarily, the *e*-values used in this analysis will be reduced by a magnitude of 1000-2000 cm^{-1} (12-24 kJ mol^{-1}) to account for the entropic stabilisation of the high-spin state. The resulting correlation between calculated and experimental T_{SCO}'s was only fair (n = 26, R^2 = 0.42, see ESI, Fig. S30), with six conspicuous outliers. These were: R = –pyrazolyl (HALC-8), –SH (HALC-15), –*cis*–CH=CHPh (HALC-19), –*cis*–CH=CH(C_6H_4-NO_2) (HALC-20), –*cis*–CH=CH(C_6H_4-CN) (HALC-21), and Y = –CO_2Et (HALC-25) (Fig. 2). Upon inspection of the complexes with aromatic substituents (HALC-8, HALC-19-21), the deviation of calculated T_{SCO} to experiment could be attributed to small differences in the metal coordination sphere brought about by intermolecular interactions between their extended aromatic substituents and the solvent, which, by definition, are not included in PBE0/def2-TZVP optimisation.

Table 3 Ligand field parameters used in calculations of T_{SCO}

Ligand Field parameters	Value (cm^{-1})
pyridine e_σ	6900
pyridine e_π	-1335
pyrazolyl e_σ	6000
pyrazolyl e_π	575
Racah B	1010
Racah C	3850
Spin orbit coupling	450

For these complexes, subsequent inspection of the experimental crystal structures showed large differences to the PBE0/def2-TZVP calculated geometries.[49] For instance, for HALC-19, the interplanar angle formed between the best-fit planes defined by the Fe and three *N*-coordinating atoms was 90.0° for the PBE0/def2-TZVP optimised structure, compared to a value of 80.2° for the crystal structure (Fig. S32), with similar differences for the other aromatic complexes. While differences between DFT optimised and XRD geometries are expected, due to packing effects and the differences between positions of nuclei and electron density, these are significant changes which will impact LFT energies. Thus, the HALC-8, HALC-19, HALC-20 and HALC-21 complexes were excluded from subsequent analysis.

Inspection of the PBE0/def2-TZVP optimised structures of the remaining complexes revealed that the HALC-25 Fe-N(p_z) bond length (1.994 Å) was reduced by >3σ compared to the averages of the other 27 DFT-optimised structures (2.001(2) Å) (Fig. S33). Whilst this difference is within the error of DFT optimisation (0.005-0.010 Å),[16] correlation of *Kestrel*-calculated T_{SCO}'s with the Fe-N(p_z) bond length (n = 23, R^2 = 0.64), shows a high sensitivity to the precise bond length such that a deviation of 0.007 Å would cause the calculated T_{SCO} to vary by ~200K. (Fig. S34). Consequently, HALC-25 was also excluded from the subsequent analysis.

The variation of T_{SCO} with the smallest N(p_z)-Fe-N(p_y) angle for each of the remaining complexes was then examined to assess the impact of the angular arrangement of the coordinating atoms (Fig. 7a, angle A). The correlation between the angle and calculated T_{SCO} was excellent save for one outlier HALC-3 (R = –CH_2SCN). Without HALC-3, n = 22, R^2 > 0.99 (Fig. S35). Examination of the PBE0/def2-TZVP optimised structure for HALC-3 showed an extra distortion in which the substituent on the pyridine ring had "folded back" towards the complex, thereby forcing the *bis*-{*bis*-(X-pyrazolyl)-Y-pyridine} ligand away from planarity (Fig. S37). This distortion is quantified in the angle formed between the Fe-N(p_y) vector and the plane described by N(p_z)-Fe-N(p_z), which has a maximum value of 0.36° (average = 0.08(11)°) for all other complexes, whereas

HALC-3 (2.55°) has a significantly larger deviation. Inclusion of dispersion (PBE0-D4), solvent (SMD) and exploration of conformers did not significantly alleviate this distortion.

Based on these differences, we concluded that the DFT-calculated structures of HALC-3, HALC-8, HALC-19-21 and HALC-25 in gas phase did not represent the experimental structures in solution and, as such, they were excluded from the remainder of the ligand field analysis. The final data set contained 20 calculated structures.

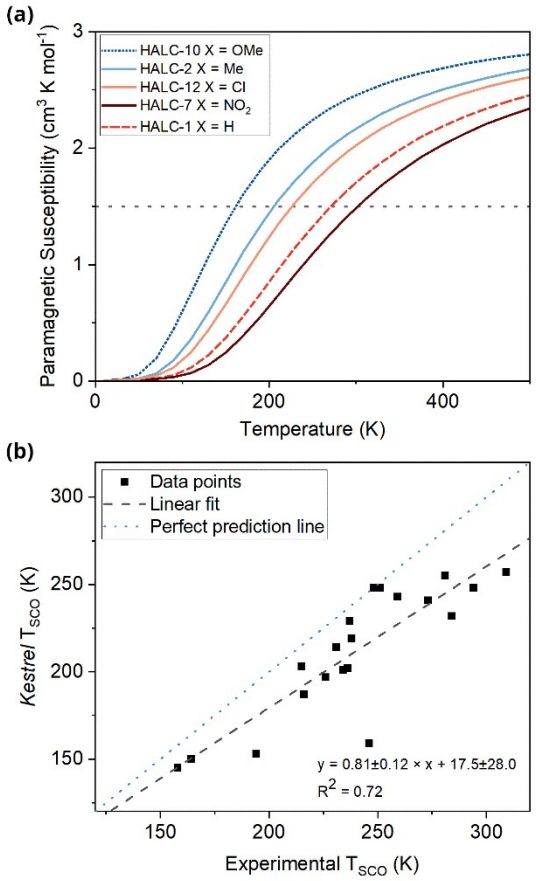

Fig. 3 (a) Susceptibility *vs* temperature plots for selected [*bis*-{*bis*-(X-pyrazolyl)-Y-pyridine}Fe(II)] PBE0/def2-TZVP optimised structures using the fixed ligand field parameters; the midpoint, $T_{1/2}$, used to extract T_{SCO}, is shown by the dashed line; (b) plot of *Kestrel* calculated *vs* experimental T_{SCO} (n = 20, R^2 = 0.72, Q^2 = 0.18)

T_{SCO} dependence on e_σ values: *Kestrel* was used to examine the sensitivity of the energy gap between the singlet (low spin Fe(II)) and quintet (high spin Fe(II)) configurations to individual ligand field parameters in the absence of spin-orbit coupling. This approach is akin to using a Tanabe-Sugano diagram. Here it was seen that the energy gap is most sensitive to Racah *B* values, but then also sensitive to both e_σ and e_π values, as expected from simple ligand field considerations (Fig. S41). Since the e_σ values for each of the separate complexes would vary depending on the substituent, individual e_σ values were determined for each of the complexes, with their relative values constrained to follow the trend expected from the differences in Hammett parameters of the substituents. As such, *Kestrel* was used in a semi-predictive sense to calculate the T_{SCO}'s of the range of complexes herein.

To obtain the variation of e_σ values with respect to their Hammett parameters (*H*), the following fitting procedure was used. In the knowledge that the pyridine acts as a π-acceptor ligand and pyrazolyl a weak π-donor, the e_σ values of each were varied to find the best fit to the known Hammett parameters (*H*) of the substituents,[39,50] starting with the fixed e_σ and e_π values from above (Fig. S42 and Fig. S43). The resulting correlations were found for pyridine: $e_\sigma(cm^{-1})$ = 6930 − 85.H, and pyrazolyl: $e_\sigma(cm^{-1})$ = 5995 + 65.H (n = 20, R^2 = 0.87 and 0.95 respectively). A final, small refinement of the *e*-value – Hammett parameter correlations was performed by maximising the correlation coefficient (n = 20, final R^2 = 0.81) between calculated and experimental SCO-temperatures, to give the following relationships: pyridine: $e_\sigma(cm^{-1})$ = 6929 − 94.H, and pyrazolyl: $e_\sigma(cm^{-1})$ = 5995 + 70.H.

Table 4 Ligand field parameters used in calculations of spin states of catalytic transition states

Ligand Field parameters	Value (cm^{-1})
Phenanthroline e_σ	7500
Phenanthroline e_π	–1000
Silane e_σ	5500
Silane e_π	0
Alkyne e_σ	7000
Alkyne e_π	–1000
Alkene e_σ	6500
Alkene e_π	–500
Hydride e_σ	8000
Hydride e_π	0
Dioxygen (side on) e_σ	6500
Dioxygen (side on) e_π	+500
Dioxygen (end on) e_σ	8000
Dioxygen (end on) e_π	–1000
Triflate e_σ	7000
Triflate e_π	0
Pyridine e_σ	7000
Pyridine e_π	–750
Bisulidine e_σ	7250
Bisulidine e_π	0
Styrene e_σ	6500
Styrene e_π	–500

Determining spin states of catalytic transition states

The structures of the catalytic intermediates and transition states were taken from the DFT calculations in the original reports, and used as input to *Kestrel*.[17,18] Initial parameter values for the ligand in each complex were taken from *e*-values of other closely-related transition metal complexes. For the exogenous ligand, parameters were also taken from known complexes, albeit less closely-related (Table 4).[51,52] These values were manually varied over a range of approximately ±10% to explore the spin states 'landscape' of the transition state. Final parameter values are summarised in the ESI, Tables S54-S56. Where the ground spin state from *Kestrel* differed from that calculated from DFT, the parameter values in *Kestrel* were varied without constraint to determine if a match could be

DOI: 10.1039/D6QI00844E

found to the spin state from DFT. The chemical feasibility of the resulting *e*-values was then assessed.

Results and Discussion

Benchmarking of DFT methods for *base_spin_dataset*

A benchmarking study by Truhlar *et al* on 14 Fe(II/III/IV) complexes indicated that B3LYP, PBE0 and M06-L are among the best performing functionals in spin state prediction.[53] In addition, TPSSh/def2-TZVP method has been employed recently by other researchers to benchmark the ground state multiplicity predictions of other methods, where no experimental data was available.[54–56] Thus, four functionals were selected for calculations of all complexes in ***base_spin_dataset*** using ORCA 6.0.1, using the def2-TZVP basis set. Grimme dispersion corrections were not included, due to conflicting assessments on their impact on SCO,[27,38] to allow their impact to be evaluated later. The selected functionals were hybrid-GGA (B3LYP, PBE0) and hybrid-meta-GGA methods (TPSSh, M06-L) which often offer a good balance between accuracy and computational cost.[16]

The four DFT methods performed well in optimising the complexes in ***base_spin_dataset***. The deviations from crystal structures are summarised in Fig. 4. On average, the bond lengths and bond angles are in good agreement with crystal structures, except for a modest general elongation of bond lengths with B3LYP/def2-TZVP.[57] PBE0 gave the closest optimised structures and more significant changes in bond angles were observed for Fe(II), Fe(III) and Co(II) complexes.

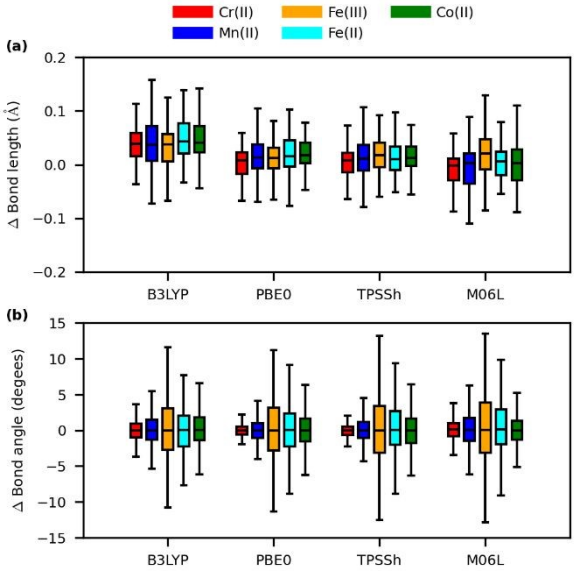

Fig. 4 Geometrical accuracy of DFT optimisation using B3LYP, PBE0, TPSSh and M06-L functionals against crystal structure data, with def2-TZVP basis set (Δ = DFT values – crystal structure values): (a) differences in metal-ligand bond lengths, and (b) differences in ligand-metal-ligand bond angles.

Table 5 P1-scores for ground state multiplicity prediction performance of DFT functionals using def2-TZVP basis set in ***base_spin_dataset***

Metal centre	B3LYP	PBE0	TPSSh	M06-L
Cr(II)	88	88	88	93
Mn(II)	93	93	83	96
Fe(III)	86	86	64	79
Fe(II)	100	96	70	87
Co(II)	93	93	93	96
All	92	91	79	90

To assess the performance of each DFT method to accurately predict the ground state multiplicity within ***base_spin_dataset***, two metrics were used: (i) the percentage of predictions with matching DFT calculated lowest energy spin state and experimentally measured spin state (P1-score), and (ii) the single point energy gap between the two lowest energy spin states in the gas phase (E1–2). These have the benefit of allowing for the potential error of each DFT method (typically >1-5 kcal·mol^{-1} with conformational and numerical noise),[16] and assessing the link between the chance of successful prediction of ground state multiplicity against the energy gap between the two lowest spin states of each complex. The results are summarised in Table 5 and Figure 5.

In general, P1-scores ranged from 64% to 100% for individual metal centres and functionals. On average, TPSSh performed the worst (79%), in contrast to the results from Ruiz and Kepp,[27,38] and B3LYP performed the best (92%), followed by M06-L (90%) and PBE0 (91%) functionals. Closer examination of spin contamination indicated that 59% of the complexes have a DFT-calculated $\langle S^2 \rangle$ value more than 10% higher than the nominated *s(s+1)* value, with higher contamination at lower spin states. This inherent issue of DFT calculations is present in all four functionals (see ESI, Fig. S2 and Table S39).

The accuracy is highly dependent on the metal centre and electron configuration, with Fe(III)/d^5 being the most difficult to predict accurately.[21,24,58] Spin -admixture and mixed spin states have previously been suggested to be a possible cause of this.[59–63] Interestingly, the Mn(II)/d^5 complexes were better predicted compared to Fe(III)/d^5 within the same DFT methods. One possible explanation is the geometries of these two metal centres (Fig. 1a). Octahedral geometry (O_h) is significantly represented in both Mn(II) and Fe(III) complexes in ***base_spin_dataset***, but the Fe(III) complexes also included a large number of 5-coordinate complexes. Examination of the rate of incorrect spin state prediction showed a significant increase for C_{4v}, D_5 and D_{5h} geometries (see ESI, Fig. S1).[23] For PBE0 calculations, incorrectly assigned multiplicities to square pyramidal and D_5/D_{5h} sandwich complexes make up just under half the errors (45%). In addition, larger differences in bond angles between DFT-optimised structures and crystal structures were observed for Fe(III) and Fe(II) complexes compared to other metal centres in ***base_spin_dataset*** (Fig. 4b). Thus, the poor performance of DFT methods in predicting the ground state multiplicity of Fe(III)/d^5 complexes is likely linked to the metal centre itself and the geometry optimisation *via* DFT methods.

View Article Online
DOI: 10.1039/D6QI00944E

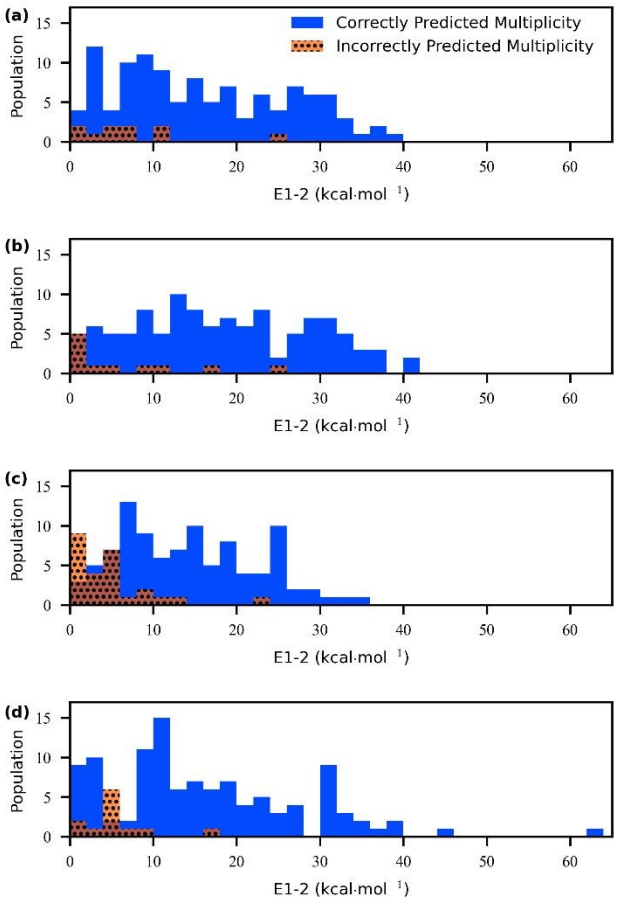

Fig. 5 Relationship between E1-2 (energy gap between the two lowest energy spin states) and incorrect predictions of ground state multiplicity by DFT methods: (a) B3LYP/def2-TZVP; (b) PBE0/def2-TZVP; (c) TPSSh/def2-TZVP; and (d) M06-L/def2-TZVP.

Lastly, the link between E1−2 and the possibility of accurate prediction of ground state multiplicity is shown in Fig. 5. Generally, a larger E1−2 value resulted in more accurate predictions of the lowest energy spin state, and a smaller E1−2 value resulted in less confidence in the DFT predicted ground state multiplicity. B3LYP, PBE0 and TPSSh functionals gave similar performances, with the Fe(III) EXUBIK complex being wrongly predicted with an E1-2 value of ≈ 26 kcal.mol^{-1}. For B3LYP, PBE0 and TPSSh, the data suggests that a threshold of E1-2 > 20 kcal.mol^{-1} may be used to assign the multiplicity prediction with some confidence based on these DFT methods. However, the poor performance of all 4 methods raised questions on their reliability in predicting spin-crossover materials and catalytic pathways, wherein the E1-2 values must be relatively small at ambient conditions. These are in agreement with the findings by Radoń *et. al.* on a smaller set of 17 transition metal complexes.[21] Thus, these 4 DFT methods were benchmarked in predicting spin-crossover temperatures (T_{SCO}) of 32 experimentally measured Fe complexes in ***T_SCO_dataset***.

Application of the best DFT methods to T_{SCO} prediction

Experimental T_{SCO} values of 32 octahedral Fe(II) complexes were curated from the literature to form ***T_SCO_dataset*** for this part of our study. The four functionals, *i.e.* B3LYP, PBE0, TPSSh and M06-L, were applied with the def2-TZVP basis set to calculate T_{SCO} using equation (1). The relatively inexpensive meta-GGA method r^{2}SCAN/def2-TZVP was also included due to its recent favourable performance in predicting spin state energies against results using TPSSh.[26] PBE0-D4 functionals were also included in order to assess the impact of dispersion correction on T_{SCO} prediction.

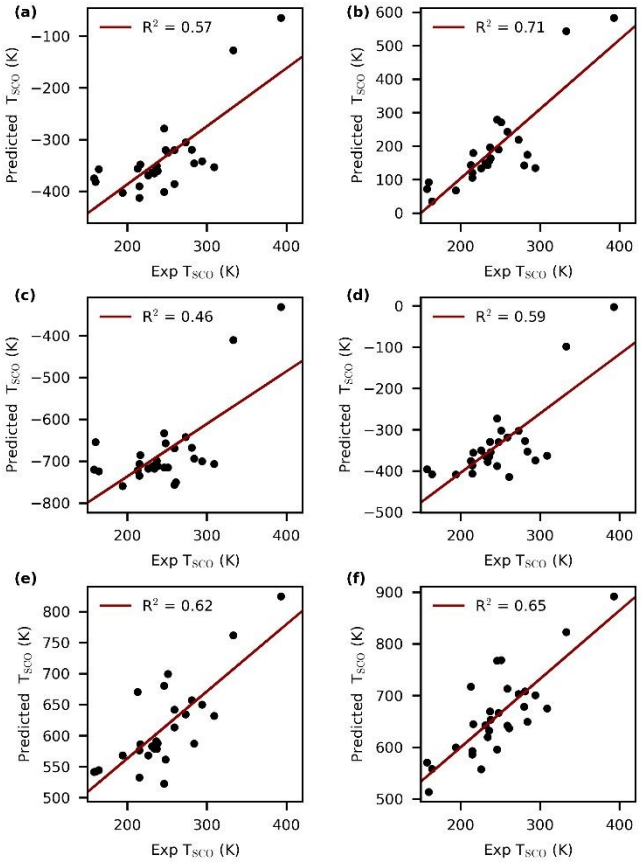

Fig. 6 Plots of predicted *vs* experimental T_{SCO} values for ***T_SCO_dataset*** without the three outliers: (a) B3LYP/def2-TZVP; (b) M06-L/def2-TZVP; (c) PBE0/def2-TZVP; (d) PBE0-D4/def2-TZVP; (e) TPSSh/def2-TZVP; and (f) r^{2}SCAN/def2-TZVP.

All six methods performed generally poorly in predicting T_{SCO}, (see ESI, section 3.2). Previous studies have suggested that the counterion, which is not included in DFT calculations, can influence T_{SCO} in solution phase,[64] but the documented changes are much smaller than the observed differences. Additionally, three complexes were often persistent outliers in more than one method (WAHKEX, KEKVIF03 and HALC-20, Fig. 2). Once these were removed, the rest of the predictions showed linear trends, albeit with large scattering, against experimental T_{SCO} values (Fig. 6). The best method was M06-L (R^2 = 0.71, Fig. 6b) and the worst method is PBE0 (R^2 = 0.46, Fig. 6c, Table S41). Surprisingly, r^{2}SCAN functionals performed relatively well compared to the more expensive methods (R^2 = 0.65, Fig. 6e). Inclusion of dispersion correction in PBE0-D4 optimisation only improved the predictions slightly (R^2 = 0.59, Fig. 6d). As the influence of solvation on optimised structures, entropy, and consequently T_{SCO}, can be significant,[65] the impact of solvation models was also assessed. Inclusion of acetone and

View Article Online
DOI: 10.1039/D6QI00844E

nitromethane as solvents, where they were used in experimental measurements, using SMD solvation model with PBE0-D4 resulted in no detectable improvement to T_{SCO} predictions (see ESI, section 3.1.5-6).

The outliers, particularly WAHKEX and KEFVIF, which are poorly predicted in most methods, were examined carefully. Both these complexes differ from the rest in ***T_SCO_dataset*** in that they contain the same monodentate ligand SCN^-. Analysis of the optimised structures of singlet and quintet states from B3LYP, PBE0 and r^{2}SCAN functionals showed that these ligands are treated differently by each of these functionals. Compared to the crystal structures, bond lengths lengthen trans to the SCN^- in B3LYP optimised structures and contract uniformly in r^{2}SCAN optimised structures. PBE0 functionals resulted in the smallest changes in bond lengths as expected. More importantly, the C-N-Fe angles of the SCN^- ligand, in the quintet state, differ significantly between B3LYP/PBE0 optimised structures and those optimised with r^{2}SCAN (ESI, Figure S25 and Table S43). More spin density is localised on the S atom of the SCN^- ligands when optimised with r^{2}SCAN, which represents more significant electron donation from the Fe centre to the SCN^- ligands. This led to the change in the hybridisation of the coordinating N-atoms.

Finally, the impact of the conditions of T_{SCO} measurements was assessed. Some correlation between the distortion of the complex's geometry from perfect octahedral geometry (*d_magnitude*) with the difference between experimental and DFT-predicted T_{SCO} values (calculated in gas phase) can be observed for those measured in solid state (ESI, Figure S24).[66] In general, DFT-optimised structures with more distortion are predicted more poorly. Solution-measured T_{SCO} values do not follow this trend, highlighting that significantly different factors influence T_{SCO} in solid and solution states.

T_{SCO} prediction with *Kestrel*

Kestrel is a computational package for ligand field calculations.[34] *Kestrel* performs multiconfigurational calculations, which, unlike the single-determinant approach typically used in DFT, means that *Kestrel* simultaneously computes the energies, configurations, and spin states of all relevant electronic states. Furthermore, the use of the effective Hamiltonian combined with the processing powers of modern desktop computers means that the calculations in *Kestrel* are carried out in real time—even for d^5 systems (where each matrix involves over 63,000 integrals). This capability allows users to explore how changes in the chemical environment affect the spectroscopy of a complex, in a way that resembles the functionality of a Tanabe–Sugano diagram.

The combination of chemically meaningful e-values and real-time configurational interaction analysis enables chemists to explore interactively the full spectrum of electronic eigenvalues and eigenfunctions. Thus, *Kestrel* provides a different approach to predicting T_{SCO} compared to both DFT and CASSCF methods.[67]

Correlation of spin crossover temperatures with ligand field parameters

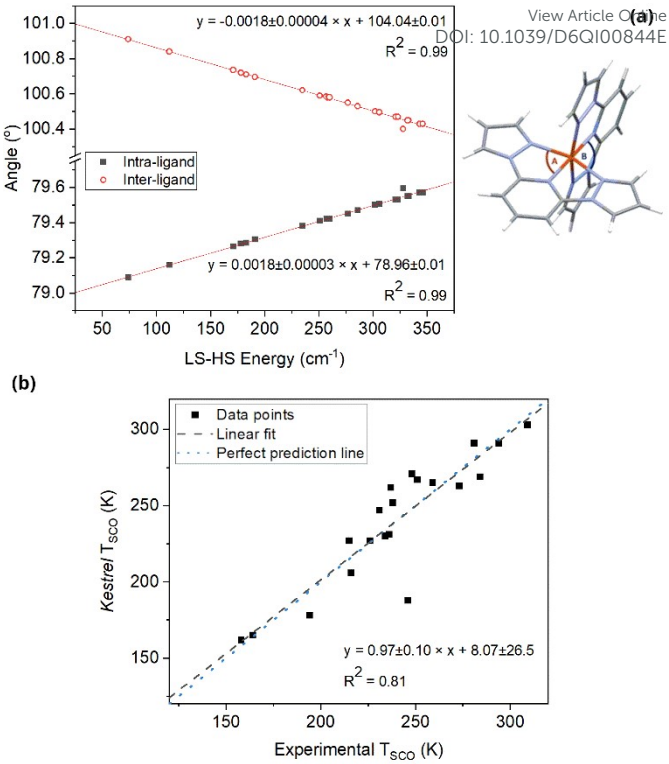

Fig. 7 (a) variation of angle A (black) and angle B (red, empty) with LS-HS energy using the fixed ligand field parameters (Table 3); (b) experimental *vs* ligand field-calculated T_{SCO}, where the ligand field strengths are linked to Hammett parameters of the substituents.

Using a ligand field approach with a fixed set of ligand field parameters (Table 3), susceptibility *vs* temperature plots were generated for each of the complexes listed (Fig. 3a) to investigate the sensitivity of T_{SCO} to the angular arrangement of the ligands. The midpoint ($T_{1/2}$) gave the T_{SCO} for each complex which was compared to the experimental value (Fig. 3b). As a first stage analysis, the correlation between experiment and theory was good (R^2 = 0.72) illustrating that ligand-field configuration-interaction analysis is able to span the eigenstates (singlet and nearby quintet) *and* their Boltzmann populations to reproduce accurately the T_{SCO} variations seen for the range of [*bis*-{*bis*-(X-pyrazolyl)-Y-pyridine}Fe(II, d^6)] complexes in ***T_SCO_dataset***. Furthermore, a MAE of 28.2 K indicates that any variation in entropy changes is small between the complexes and can be accounted for with the initial *e* parameters used in this analysis. A weak predictive squared correlation coefficient (Q^2 = 0.18),[68] however, shows this analysis to have only limited capability to calculate T_{SCO} values *a priori*. This is due to a systematic underestimation of T_{SCO}'s compared to experimental values when using the fixed set of ligand field parameters (Fig. 3b, dashed line), see section below. Since singlet-quintet gap of this range of complexes spans almost 300 cm^{-1}, the small angular variations between the structures of complexes in the low-spin state are one of the principal contributors, if not the principal contributor, to the differences in T_{SCO}'s between the complexes. This conclusion runs somewhat counter to existing analyses of these complexes which relate the differences in coordinating strengths of the

View Article Online DOI: 10.1039/D6QI00844B

ligands as the main means by which the T_{SCO}'s vary.[39,69] Indeed, the sensitivity of T_{SCO} to small angular variations can be seen from both the dependency of the T_{SCO}'s on the N(p_y)-Fe-N(p_z) angles (Fig. S35) and the variation plot in Fig. 7a. The latter calculates the singlet-quintet gap as a function of the intra-ligand (angle A) and inter-ligand (angle B) angles, showing that even small angular variations (<0.6°) of each of these can span almost 300 cm^{-1} in the singlet-quintet gap. This effect was observed and rationalised in earlier studies by us and others.[70,71] Whilst the angular arrangement of the high-spin state is different from the low-spin state, analysis of the variation in the same angles for the high-spin (PBE0) structures revealed a much weaker correlation (Fig. S36). Hence, the change in geometry and thus the T_{SCO} between complexes is principally governed by the angular arrangement of the low-spin state that is considered in *Kestrel's* calculations, with the high-spin angles offset by a constant value (~6.5°, Fig. S39). Indeed, the anticipated error from neglecting the high-spin geometry is 50 K, i.e. ±25 K, which is within the MAE of 28.2 K between experimental and calculated T_{SCO} in *Kestrel's* analysis using fixed *e*-values.

Contribution of σ-donating properties of ligands to spin-crossover temperature

Notwithstanding the ability of *Kestrel* to delineate the principal causes of variation in T_{SCO} from a simple first analysis, it was evident that the ligating properties of each ligand within the range of complexes was also an important factor in using *Kestrel* to model T_{SCO}'s. To address this issue, two approaches were adopted to assess the extent of variations in ligand field strengths. In the first approach, the *σ*-donating strengths of the pyridine and pyrazolyl ligands were adjusted to give an exact match between calculated and experimental T_{SCO}'s. This could be achieved with only a modest change, the difference between the largest and smallest values, in e_σ values (± 47 cm^{-1} for pyridine and ± 38 cm^{-1} for pyrazolyl. This indicated that the precise ligand field strength is a small factor in the observed variation in T_{SCO} and further supports that variations in entropy changes and the high-spin geometry are small between the complexes. However, this approach lacks a predictive ability since e_σ values are manually varied to fit known data.

Thus, in a second approach, e_σ values for each ligand were determined *a priori* from their known Hammett parameters (see ESI, Table S52), which were then used to calculate T_{SCO} for each complex, thus eliminating the need to fit to experimental data. The correlation with experimental values is shown in Fig. 7b. and is good (R^2 = 0.81, Q^2 = 0.78) with one outlier (R = –SH). The e_σ values used in this second analysis again show only modest ranges (± 54 cm^{-1} for pyridine and ± 40 cm^{-1} for pyrazolyl). Therefore, both approaches show that the relative ligating strengths of the different ligands is only a small contributor to the individual T_{SCO}. However, a significant improvement in the Q^2 value from 0.18 to 0.78 when determining e_σ values from their Hammett parameters, shows the consideration of *σ*-donor strength to be important in enhancing the predictive capacity of the ligand field approach used within *Kestrel*. By leveraging derived Hammett parameters,[50] this approach can be extended to predict the T_{SCO} of un-synthesised substituted derivates of a common ligand scaffold, providing a valuable computational tool to aid in tuning the electronic properties of a complex and its precise SCO characteristics.

These results indicate that changing the substituent only slightly modifies the relative donor strengths of the pyrazolyl and pyridine ligands, the principal cause in variation of T_{SCO} between the complexes being the effect that the different substituents have on the angular distribution of the ligating atoms within the individual complexes. The change in angular arrangement of ligating atoms as a function of substituent can be rationalised as follows: increasing the strength of the *σ*-donation of pyrazolyl in comparison to that of pyridine enhances the pyrazolyl ligand's overlap with the 4*p* valence orbitals of the metal ion. This leads to an angular dependence of the coordinating atoms as a function of substituent. The result is a change in the intra- and inter-ligand bite angles, both of which are sensitive determinants of the T_{SCO} of the complex. This is the principal mechanism by which the T_{SCO} varies as a function of substituent. Thus, the most effective approach to prediction of trends in spin states and T_{SCO} of base metal complexes is to employ reliable DFT-optimised geometries in *Kestrel*.

Application of Kestrel to PBE0-D4 structures

Given the sensitivity of *Kestrel* to the angular arrangement of the ligating atoms, PBE0-D4/def2-TZVP optimised geometries of complexes in ***T_SCO_dataset*** were employed to evaluate improvement in the predictions of T_{SCO}. Using the parameter values in Table 3, a significantly better Pearson correlation coefficient value was obtained, (R^2 = 0.57, *n* = 26, Fig. S31), compared to the value achieved using PBE0/def2-TZVP optimised geometries (R^2 = 0.42, *n* =26, Fig. S30).

Analysis of the PBE0-D4 optimised structures showed the same reduced bond length for HALC-25 and "folding back" of the CH_2SCN substituent for HALC-3 as discussed for the PBE0 structures. Thus, these outliers were excluded from T_{SCO} prediction with *Kestrel*, giving a good correlation between experimental and calculated T_{SCO} (*n*=24, R^2 = 0.64, Fig. 8a). For the complexes with extended aromatic substituents (HALC-8 and HALC-19-21), PBE0-D4 shows a greater distortion of interplanar angle from 90° than for the PBE0 optimised structures: for instance, the interplanar angle in HALC-20 is 89.7° compared to 90.0° for the PBE0 optimised structure, and 86.0° for the crystal structure.[49] Including dispersion correction evidently results in a more accurate treatment of the complexes with extended aromatic substituents and hence prediction of T_{SCO} by *Kestrel* (see ESI, Table S51).

Whilst including dispersion correction in DFT optimisations gives a more accurate treatment of the aromatic-substituted complexes, the fitted linear curve in Fig. 8a has a slope significantly different from the desired value of 1. This likely reflects a global change in the donor properties of the ligating atoms and/or the entropy-enthalpy compensation brought about by the change to the PBE0-D4 functionals. Consequently, this was corrected for by reducing the initial e_σ value for pyridine to 6860 cm^{-1} (from 6900 cm^{-1}) and that for pyrazolyl to 5980 cm^{-1} (from 6000 cm^{-1}). Exact e_σ values were then determined for each complex using the Hammett correlations derived in the previous analysis: pyridine $e_\sigma(cm^{-1})$ = 6860 − 94.H and pyrazolyl: $e_\sigma(cm^{-1})$ = 5980 + 70.H (see ESI, Table S53). This analysis resulted in a significant improvement in the ability of *Kestrel* to predict the exact T_{SCO} (R^2 = 0.71, Q^2 = 0.57, RMSE = 23.3 K, n = 24, Fig. 8b).

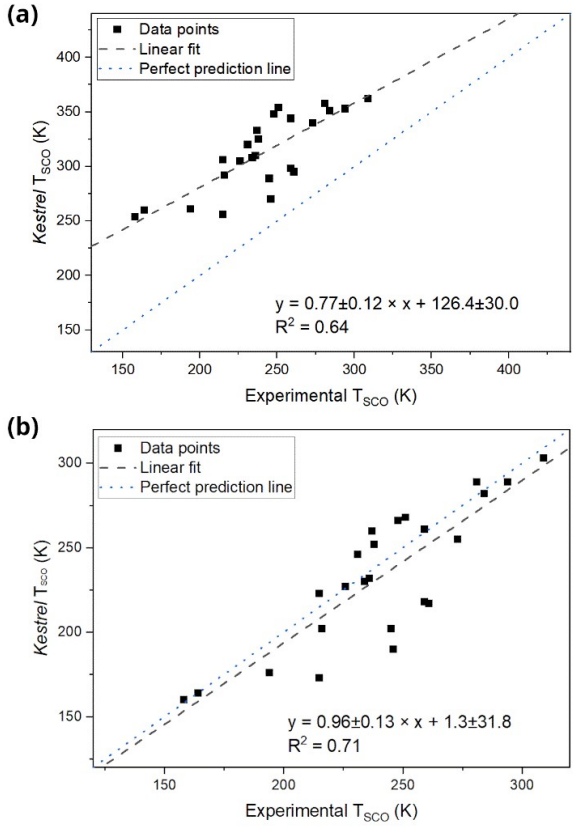

Fig. 8 (a) Experimental *vs Kestrel*-calculated T_{SCO} using PBE0-D4 optimised geometries (n = 24, R^2 = 0.64); (b) Experimental *Kestrel*-calculated T_{SCO} using PBE0-D4 optimised geometries where e_σ values are linked to the Hammett parameters of the substituents (n = 24, R^2 = 0.71)

Whilst this is a weaker correlation than those of predictions using PBE0 structures (R^2 = 0.81), it should be emphasised that this analysis includes 4 more complexes, due to the improved geometric accuracy of PBE0-D4 functionals. A like-for-like comparison, with HALC-8 and HALC-19-21 included for PBE0 geometries, gives a weaker correlation and higher RMSE (R^2 = 0.56, Q^2 = 0.27, RMSE = 30.6 K, n = 24), supporting a clear improvement in predictive ability with the PBE0-D4 structures. This highlights the sensitivity of spin crossover to the precise nature of the ligand field surrounding the metal centre.

Spin state prediction for catalytic intermediates and transition states with *Kestrel*

Kestrel was used to evaluate two catalytic reactions where spin crossover has been reported to be part of the mechanism based on DFT calculations.[17,18] These are Fe(II)/Fe(III) catalysed C(sp^3)–H silylation and oxidation of styrenes, reactions of great industrial interest which also highlight the challenges in determining the spin state of the relevant catalytic species. The DFT methods employed were ωB97XD/def2-TZVP(SMD:THF)//ωB97XD/6-31G*-TZVP and UB3LYP/LanL2DZ /cc-pVTZ//UB3LYP/LanL2DZ/6-31G*. Based on the unconvincing performance of most DFT functionals in predicting the lowest energy spin states of Fe(II) and Fe(III) complexes (Table 5) and in predicting T_{SCO} of Fe(II) complexes (Fig 6), we decided to carry out an independent assessment of the key catalytic species and transition states in these two reactions with *Kestrel* (Scheme 1). The results in the last sections have highlighted the importance of angular arrangement of the ligands on the spin state of Fe(II) species, and we expect this to be even more critical in catalytic transition states, leading to the evaluation of *Kestrel's* predictions against those of DFT methods.

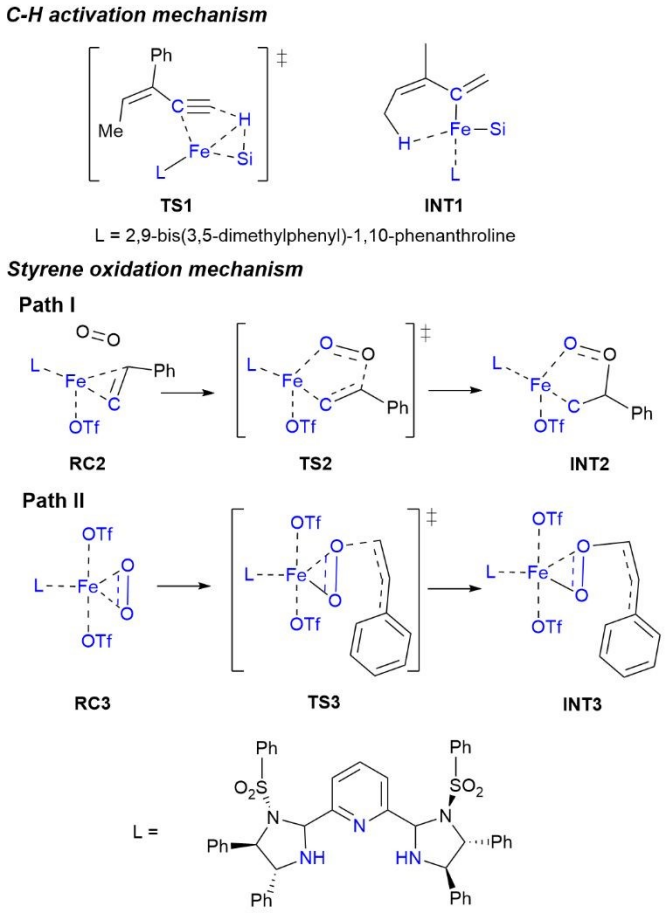

Scheme 1 Structures of calculated transition states and intermediates. Ligand field calculations were performed on the coordinating atoms and the atoms highlighted in blue.

Allylic C(sp^3)-H silylation/alkene hydrosilation: This reaction is catalysed by a Fe(II)/1,10-phenanthroline complex. The

View Article Online
DOI: 10.1039/D6QI00841F

previously reported spin crossover step is between a triplet **TS1** and a quintet **INT1** (Scheme 1).[18] Thus, the energies of the singlet, triplet and quintet states for **TS1** and **INT1**, were calculated using *Kestrel* and compared to those from the original publication.

Whilst the quintet ground spin state of **INT1** is in agreement with that from DFT calculations, **TS1** is predicted to be in a quintet ground state instead of a triplet ground state. To assess the robustness of these results, variation diagrams were calculated (Fig. S45). Despite varying the ligand field parameters over a wide range, the quintet state remained around 3000 cm^{-1} above the triplet ground state, even at chemically unfeasible *e*-values. This indicates that the disagreement between *Kestrel* and DFT is likely not a result of poor parameterisation in the ligand field calculations or of a restricted basis set. It is notable that DFT calculations differ from those in *Kestrel* as the former includes significant covalent overlap between ligand orbitals and metal-based 3d orbitals, which necessarily can lead to large ligand-field splitting. In this case, such overlap could explain why DFT calculations predict a triplet rather than quintet ground state for **TS1**. While such covalent interactions will always contribute to the energy of the metal-based *d* orbitals, how much of this is overestimated by DFT calculations because of the self-interaction error which is a feature of such calculations is unknown.

As calculations in *Kestrel* cover all possible spin states at the metal, it is revealed that the quintet ground state in **TS1** contains approximately 0.5% triplet character *via* spin-orbit coupling (Fig. 9a) and also that there is a thermally accessible singlet state (950 cm^{-1} at 298 K) with *ca.* 5% triplet character. Whether these admixtures of triplet state into the ground state or the thermally accessible singlet/triplet state offer alternative pathways to the reactive triplet surface is an open question. A similar argument has recently been made for the reactive intermediates in other Fe complexes and Fe-based P450 enzymes.[72,73]

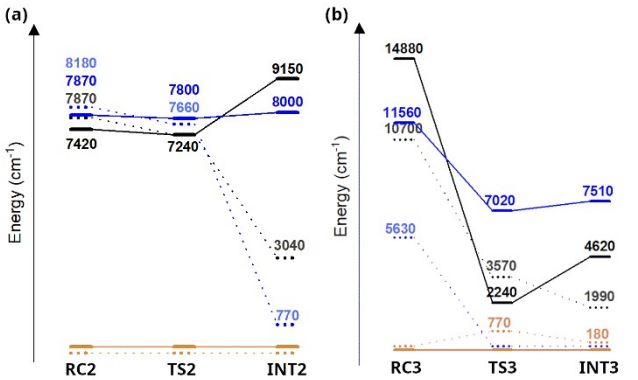

Fig. 9 (a) configurational mixing of lowest energy quintet (left), singlet (middle) and triplet state (right). Singlet (grey), triplet (blue) and quintet (orange) configuration contributions to each state are shown. (b) energy profile of literature DFT calculated spin-state energies (dashed lines) and Kestrel calculated spin state energies (solid lines) for the singlet (black), triplet (blue) and quintet (orange) states for **TS1** and **INT1**

Fe(III)-catalysed styrene oxidation: This reaction is catalysed by a Fe(III) catalyst with a tridentate ligand. Two mechanisms were proposed based on DFT calculations: (i) **Path I** which starts with olefin coordination, and (ii) **Path II** which starts with dioxygen coordination (Scheme 1).[17] DFT calculations suggested that a spin-crossover step from octet **RC3** (a combination of sextet $3d^5$ complex and triplet dioxygen) to sextet **TS3** is a key step in the dominant catalytic cycle.

The energies of the doublet, quartet and sextet states for **RC2**/**RC3**, **TS2**/**TS3** and **INT2**/**INT3** were calculated using *Kestrel*. For **Path I**, ligand field calculations agreed with DFT-calculated energies for **RC2** and **TS2**, both of which predict a sextet ground state, albeit with small differences on the exact energies of the excited doublet and quartet states. **INT2** was also found to have a sextet ground state, but DFT calculations placed the excited doublet and quartet states much closer in energy to the sextet ground state than in *Kestrel*'s calculations. For **Path II**, both methods of calculations show the energetic differences between the different spin states to be much lower for TS3/INT3 than those of **Path I**. However, the sextet state is predicted to be the ground state for all transition states and intermediates by ligand field calculations, in contrast to reported DFT results (Fig. 10) where **TS3** and **INT3** have a triplet ground state. Thus, *Kestrel* predicted no spin crossover in the catalytic cycles of this reaction.

The differences between *Kestrel* and DFT predictions may be attributed to the different ways in which covalency is handled. In this regard, the presence of a S ≠ 0 "O_2 ligand" in the coordination sphere brings not only the possibility of enhanced covalent bonding to the metal through its high-lying π^* valence orbitals, but also exchange interactions between ligand and metal. How much the explicit lack of accommodating these factors in the ligand field calculations affects the results is unknown. However, since there is broad agreement between the energy levels calculated by both methods, the effect may be small.

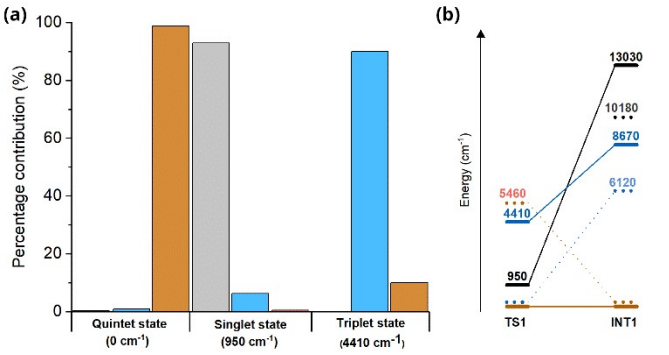

Fig. 10 (a) Energy profile of DFT calculated spin-state energies (dashed lines) and *Kestrel* calculated spin state energies (solid lines) for **Path I**; (b) energy profile of DFT calculated spin-state energies (dashed lines) and *Kestrel* calculated spin state energies (solid lines) for **Path II**. Energies are shown for doublet (black), quartet (blue) and sextet (orange) states.

Conclusion

Our DFT benchmarking of the lowest energy spin state of 127 base metal complexes in ***base_spin_dataset*** showed that B3LYP, PBE0, TPSSh and M06-L functionals perform unreliably for all metals, particularly when the energy gap between the two lowest energy spin states is small. On average B3LYP, PBE0

and M06-L are better functionals (91% accurate for the lowest energy spin state) than TPSSh. PBE0/def2-TZVP is the most reliable method for geometrical optimisation, albeit still with significant differences in bond angles, when compared to crystal structure of the complexes. These shortcomings are reflected in poor performance in predicting the spin-crossover temperature T_{SCO} of Fe(II) complexes in ***T_SCO_dataset*** with optimised geometries from PBE0/def2-TZVP.

Predictions of T_{SCO} using ligand field theory with *Kestrel* gave much better results, due to its multiconfigurational calculations and approach of fitting ligand field parameters to experimental data, with the correlation of e_σ values with the Hammett parameter of each substituent providing an effective means of predicting T_{SCO} for range of substituents within a common ligand framework, with potential for extension to various novel substituted complexes. *Kestrel* also revealed the high sensitivity of the T_{SCO} value for a Fe(II) complex to even small changes in the angular distribution of ligands, signifying how *Kestrel*'s ligand field approach permits greater insight into the electronic and geometrical nature of a system than the *'black-box'* calculations of DFT. Both findings provide greater understanding of how T_{SCO} is affected by the surrounding coordination environment. The approach was extended to two literature examples of catalytic cycles which contain DFT-supported spin-crossover mechanistic steps. In both cases, *Kestrel* agrees with DFT on the lowest energy spin states of the starting intermediate, but indicates no spin-crossover in the relevant mechanistic steps.

Thus, DFT prediction of T_{SCO} should not be used as the basis of assessment of SCO events, including spin-crossover catalysis. These results also highlight the need to include intermolecular interactions in future predictions in solid state. Such interactions can be either structural or electronic in origin, both of which would have a significant impact on the T_{SCO} of a complex.

Author contributions

BNN, MAH, YX, MAB and PHW provided direction and supervision in the project. SM performed DFT calculations and BSG performed *Kestrel* calculations. Data analysis and plotting were carried out by SM, BSG and BNN. s

Conflicts of interest

There are no conflicts to declare.

Data Avaliablity

Data for this article, including the datasets (***base_spin_dataset*** and ***T_SCO_dataset***) and the DFT optimised structures, are available at Zenodo at https://zenodo.org/records/18182735. The python codebase and GUI for Kestrel can be made available, free of charge, by emailing chem-kestrel@york.ac.uk.

Acknowledgements

PHW, MAB and BSG acknowledge the EPSRC for the provision of a studentship to BG. SM thanks GoldenKeys High-Tech Materials Co., Ltd. (91520900MA6DL1ER7N) and University of Leeds for his studentship. AG acknowledges funding from the EPSRC (EP/X021033/1). This work was undertaken on the ARC4 and Aire HPC systems at the University of Leeds, UK. We thank Department of Science and Technology of Guizhou Province, Guizhou Service Center For Academician Expert, and Mr. Songlin Liu from Weng Fu Research Institute of Technology for their kind contribution to this collaboration.

References

1 M. L. Clapson, C. S. Durfy, D. Facchinato and M. W. Drover, Base metal chemistry and catalysis, *Cell Reports Phys. Sci.*, 2023, **4**, 101548.

2 A. R. Ickes, M. C. Haibach, N. G. W. Cowper and T. S. Ahmed, Recent Advances in Nonprecious Metal Catalysis, *Org. Process Res. Dev.*, 2024, **28**, 937–948.

3 A. Fürstner, Iron Catalysis in Organic Synthesis: A Critical Assessment of What It Takes To Make This Base Metal a Multitasking Champion, *ACS Cent. Sci.*, 2016, **2**, 778–789.

4 Y. Gong, J. Hu, C. Qiu and H. Gong, Insights into Recent Nickel-Catalyzed Reductive and Redox C–C Coupling of Electrophiles, C(sp3)–H Bonds and Alkenes, *Acc. Chem. Res.*, 2024, **57**, 1149–1162.

5 Z. W. Davis-Gilbert and I. A. Tonks, Titanium redox catalysis: insights and applications of an earth-abundant base metal, *Dalt. Trans.*, 2017, **46**, 11522–11528.

6 R. M. Bullock, J. G. Chen, L. Gagliardi, P. J. Chirik, O. K. Farha, C. H. Hendon, C. W. Jones, J. A. Keith, J. Klosin, S. D. Minteer, R. H. Morris, A. T. Radosevich, T. B. Rauchfuss, N. A. Strotman, A. Vojvodic, T. R. Ward, J. Y. Yang and Y. Surendranath, Using nature's blueprint to expand catalysis with Earth-abundant metals, *Science (80-.).*, 2020, **369**, eabc3183.

7 V. Wellm, C. Näther and R. Herges, Molecular Spin State Switching and Photochromism in the Red and Near Infrared with Ni(II) Chlorin and Ni(II) Bacteriochlorin, *J. Org. Chem.*, 2021, **86**, 9503–9514.

8 S. Hayami, S. M. Holmes and M. A. Halcrow, Spin-state switches in molecular materials chemistry, *J. Mater. Chem. C*, 2015, **3**, 7775–7778.

9 G. Yang, Z.-P. Ni and M.-L. Tong, Recent advances in metal cluster-containing spin-crossover coordination compounds, *Coord. Chem. Rev.*, 2024, **521**, 216146.

10 K. Ridier, A.-C. Bas, Y. Zhang, L. Routaboul, L. Salmon, G. Molnár, C. Bergaud and A. Bousseksou, Unprecedented switching endurance affords for high-resolution surface temperature mapping using a spin-crossover film, *Nat. Commun.*, 2020, **11**, 3611.

11 N. A. A. M. Amin, S. M. Said, M. F. M. Salleh, A. M. Afifi, N. M. J. N. Ibrahim, M. M. I. M. Hasnan, M. Tahir and N. Z. I. Hashim, Review of Fe-based spin crossover metal

complexes in multiscale device architectures, *Inorganica Chim. Acta*, 2023, **544**, 121168.

12 L. Sun, A. Rotaru and Y. Garcia, A non-porous Fe(II) complex for the colorimetric detection of hazardous gases and the monitoring of meat freshness, *J. Hazard. Mater.*, 2022, **437**, 129364.

13 K. Ridier, A.-C. Bas, Y. Zhang, L. Routaboul, L. Salmon, G. Molnár, C. Bergaud and A. Bousseksou, Unprecedented switching endurance affords for high-resolution surface temperature mapping using a spin-crossover film, *Nat. Commun.*, 2020, **11**, 3611.

14 M. Roemelt and D. A. Pantazis, Multireference Approaches to Spin-State Energetics of Transition Metal Complexes Utilizing the Density Matrix Renormalization Group, *Adv. Theory Simulations*, 2019, **2**, 1800201.

15 M. Drosou, C. A. Mitsopoulou and D. A. Pantazis, Reconciling Local Coupled Cluster with Multireference Approaches for Transition Metal Spin-State Energetics, *J. Chem. Theory Comput.*, 2022, **18**, 3538–3548.

16 M. Bursch, J.-M. Mewes, A. Hansen and S. Grimme, Best-Practice DFT Protocols for Basic Molecular Computational Chemistry, *Angew. Chemie Int. Ed.*, 2022, **61**, e202205735.

17 Y. Jiang, X. Zhang, Q. Mao, H. Tan, X. Li, G. Chen and Z. Jia, A theoretical study on oxidative cleavage of olefins to carbonyls catalysed by Fe(iii)-PyBisulidine, *Dalt. Trans.*, 2017, **46**, 3825–3832.

18 P. He, M.-H. Guan, M.-Y. Hu, Y.-J. Zhou, M.-Y. Huang and S.-F. Zhu, Iron-Catalyzed Allylic C(sp3)−H Silylation: Spin-Crossover-Efficiency-Determined Chemoselectivity, *Angew. Chemie Int. Ed.*, 2024, **63**, e202402044.

19 K.-M. Zhao, D.-X. Wu, W.-K. Wu, J.-B. Nie, F.-S. Geng, G. Li, H.-Y. Shi, S.-C. Huang, H. Huang, J. Zhang, Z.-Y. Zhou, Y.-C. Wang and S.-G. Sun, Identifying high-spin hydroxyl-coordinated Fe3+N4 as the active centre for acidic oxygen reduction using molecular model catalysts, *Nat. Catal.*, 2025, **8**, 422–435.

20 H. Neugebauer, B. Bädorf, S. Ehlert, A. Hansen and S. Grimme, High-throughput screening of spin states for transition metal complexes with spin-polarized extended tight-binding methods, *J. Comput. Chem.*, 2023, **44**, 2120–2129.

21 M. Radoń, G. Drabik, M. Hodorowicz and J. Szklarzewicz, Performance of quantum chemistry methods for a benchmark set of spin-state energetics derived from experimental data of 17 transition metal complexes (SSE17), *Chem. Sci.*, 2024, **15**, 20189–20204.

22 R. J. Deeth and N. Fey, The performance of nonhybrid density functionals for calculating the structures and spin states of Fe(II) and Fe(III) complexes, *J. Comput. Chem.*, 2004, **25**, 1840–1848.

23 G. Drabik, J. Szklarzewicz and M. Radoń, Spin-state energetics of metallocenes: How do best wave function and density functional theory results compare with the experimental data?, *Phys. Chem. Chem. Phys.*, 2021, **23**, 151–172.

24 O. S. Siig and K. P. Kepp, Iron(II) and Iron(III) Spin Crossover: Toward an Optimal Density Functional, *J. Phys. Chem. A*, 2018, **122**, 4208–4217.

25 V. Vennelakanti, M. G. Taylor, A. Nandy, C. Duan and H. J. Kulik, Assessing the performance of approximate density functional theory on 95 experimentally characterized Fe(II) spin crossover complexes, *J. Chem. Phys.*, 2023, **159**, 24120.

26 S. Gómez-Coca and E. Ruiz, Accurate state energetics in spin-crossover systems using pure density functional theory, *Dalt. Trans.*, 2024, **53**, 11895–11902.

27 J. Cirera, M. Via-Nadal and E. Ruiz, Benchmarking Density Functional Methods for Calculation of State Energies of First Row Spin-Crossover Molecules, *Inorg. Chem.*, 2018, **57**, 14097–14105.

28 H. Neugebauer, B. Bädorf, S. Ehlert, A. Hansen and S. Grimme, High-throughput screening of spin states for transition metal complexes with spin-polarized extended tight-binding methods, *J. Comput. Chem.*, 2023, **44**, 2120–2129.

29 V. Vennelakanti, I. B. Kilic, G. G. Terrones, C. Duan and H. J. Kulik, Machine Learning Prediction of the Experimental Transition Temperature of Fe(II) Spin-Crossover Complexes, *J. Phys. Chem. A*, 2024, **128**, 204–216.

30 A. Albavera-Mata, P. Prakash, J. B. Gibson, E. Fonseca, S. Ren, X.-G. Zhang, H.-P. Cheng, M. Shatruk, S. B. Trickey and R. G. Hennig, Discovery of Spin-Crossover Materials with Equivariant Graph Neural Networks and Relevance-Based Classification, *J. Chem. Theory Comput.*, 2025, **21**, 3913–3921.

31 P. Morgante and R. Peverati, Comparison of the Performance of Density Functional Methods for the Description of Spin States and Binding Energies of Porphyrins, 2023, DOI: 10.3390/molecules28083487.

32 M. G. Taylor, T. Yang, S. Lin, A. Nandy, J. P. Janet, C. Duan and H. J. Kulik, Seeing Is Believing: Experimental Spin States from Machine Learning Model Structure Predictions, *J. Phys. Chem. A*, 2020, **124**, 3286–3299.

33 S. Mugiraneza and A. M. Hallas, Tutorial: a beginner's guide to interpreting magnetic susceptibility data with the Curie-Weiss law, *Commun. Phys.*, 2022, **5**, 95.

34 P. Comba, G. Nunn, F. Scherz and P. H. Walton, Intermediate-spin iron(iv)-oxido species with record reactivity, *Faraday Discuss.*, 2022, **234**, 232–244.

35 P. He and S.-F. Zhu, Spin Crossover and Its Application in Organometallic Catalysis: Concepts and Recent Progress, *Chem. – A Eur. J.*, 2024, **30**, e202403437.

36 C. R. Groom, I. J. Bruno, M. P. Lightfoot and S. C. Ward, The Cambridge Structural Database, *Acta Crystallogr. Sect. B*, 2016, **72**, 171–179.

37 D. Vidal, J. Cirera and J. Ribas-Arino, Accurate calculation of spin-state energy gaps in Fe(iii) spin-crossover systems using density functional methods, *Dalt. Trans.*, 2021, **50**, 17635–17642.

38 K. P. Kepp, Theoretical Study of Spin Crossover in 30 Iron Complexes, *Inorg. Chem.*, 2016, **55**, 2717–2727.

39 L. J. Kershaw Cook, R. Kulmaczewski, R. Mohammed, S. Dudley, S. A. Barrett, M. A. Little, R. J. Deeth and M. A. Halcrow, A Unified Treatment of the Relationship Between

Ligand Substituents and Spin State in a Family of Iron(II) Complexes, *Angew. Chemie Int. Ed.*, 2016, **55**, 4327–4331.

40 F. Neese, Software Update: The ORCA Program System—Version 6.0, *WIREs Comput. Mol. Sci.*, 2025, **15**, e70019.

41 M. Gerloch and R. G. Woolley, Is the angular overlap model chemically significant?, *J. Chem. Soc. Dalt. Trans.*, 1981, 1714–1717.

42 R. G. Woolley, The angular overlap model in ligand field theory, *Mol. Phys.*, 1981, **42**, 703–720.

43 M. Sorai, Calorimetric Investigations of Phase Transitions Occurring in Molecule-Based Materials in Which Electrons Are Directly Involved, *Bull. Chem. Soc. Jpn.*, 2001, **74**, 2223–2253.

44 K. P. Kepp, Consistent descriptions of metal–ligand bonds and spin-crossover in inorganic chemistry, *Coord. Chem. Rev.*, 2013, **257**, 196–209.

45 M. Radoń, Benchmarks for transition metal spin-state energetics: why and how to employ experimental reference data?, *Phys. Chem. Chem. Phys.*, 2023, **25**, 30800–30820.

46 G. Brehm, M. Reiher and S. Schneider, Estimation of the Vibrational Contribution to the Entropy Change Associated with the Low- to High-Spin Transition in Fe(phen)2(NCS)2 Complexes: Results Obtained by IR and Raman Spectroscopy and DFT Calculations, *J. Phys. Chem. A*, 2002, **106**, 12024–12034.

47 M. Gerloch, *Magnetism and ligand-field analysis*, Cambridge University Press, Cambridge, 1983.

48 R. J. Deeth, M. A. Halcrow, L. J. Kershaw Cook and P. R. Raithby, Ab Initio Ligand Field Molecular Mechanics and the Nature of Metal-Ligand π-Bonding in Fe(II) 2,6-di(pyrazol-1-yl)pyridine Spin Crossover Complexes, *Chem. – A Eur. J.*, 2018, **24**, 5204–5212.

49 K. Takahashi, Y. Hasegawa, R. Sakamoto, M. Nishikawa, S. Kume, E. Nishibori and H. Nishihara, Solid-State Ligand-Driven Light-Induced Spin Change at Ambient Temperatures in Bis(dipyrazolylstyrylpyridine)iron(II) Complexes, *Inorg. Chem.*, 2012, **51**, 5188–5198.

50 C. Hansch, A. Leo and R. W. Taft, A survey of Hammett substituent constants and resonance and field parameters, *Chem. Rev.*, 1991, **91**, 165–195.

51 A. Bencini, C. Benelli and D. Gatteschi, The angular overlap model for the description of the paramagnetic properties of transition metal complexes, *Coord. Chem. Rev.*, 1984, **60**, 131–169.

52 P. E. Hoggard, eds. D. M. P. Mingos and T. Schönherr, Springer Berlin Heidelberg, Berlin, Heidelberg, 2004, pp. 37–57.

53 P. Verma, Z. Varga, J. E. M. N. Klein, C. J. Cramer, L. Que and D. G. Truhlar, Assessment of electronic structure methods for the determination of the ground spin states of Fe(ii), Fe(iii) and Fe(iv) complexes, *Phys. Chem. Chem. Phys.*, 2017, **19**, 13049–13069.

54 D. Mejía-Rodríguez and S. B. Trickey, Spin-Crossover from a Well-Behaved, Low-Cost meta-GGA Density Functional, *J. Phys. Chem. A*, 2020, **124**, 9889–9894.

55 S. Gómez-Coca and E. Ruiz, Accurate state energetics in spin-crossover systems using pure density functional theory, *Dalt. Trans.*, 2024, **53**, 11895–11902.

56 S. Gómez-Coca and E. Ruiz, Benchmarking Periodic Density Functional Theory Calculations for Spin-State Energies in Spin-Crossover Systems, *Inorg. Chem.*, 2024, **63**, 13338–13345.

57 J. Moto Ongagna, A. D. Tamafo Fouegue, B. Ateba Amana, G. Mouzong D'ambassa, J. Zobo Mfomo, L. Mbaze Meva'A and D. Bikele Mama, B3LYP, M06 and B3PW91 DFT assignment of nd8 metal-bis-(N-heterocyclic carbene) complexes, *J. Mol. Model.*, 2020, **26**, 246.

58 M. Radoń, Predicting spin states of iron porphyrins with DFT methods including crystal packing effects and thermodynamic corrections, *Phys. Chem. Chem. Phys.*, 2024, **26**, 18182–18195.

59 R. Weiss, A. Gold and J. Terner, Cytochromes c': Biological Models for the S = 3/2,5/2 Spin-State Admixture?, *Chem. Rev.*, 2006, **106**, 2550–2579.

60 M. Viciano-Chumillas, G. Blondin, M. Clémancey, J. Krzystek, M. Ozerov, D. Armentano, A. Schnegg, T. Lohmiller, J. Telser, F. Lloret and J. Cano, Single-Ion Magnetic Behaviour in an Iron(III) Porphyrin Complex: A Dichotomy Between High Spin and 5/2–3/2 Spin Admixture, *Chem. – A Eur. J.*, 2020, **26**, 14242–14251.

61 M. D. Fryzuk, D. B. Leznoff, E. S. F. Ma, S. J. Rettig and V. G. Young, Synthesis, Structure, and Reactivity of Paramagnetic Iron(II) and Iron(III) Amidodiphosphine Complexes, *Organometallics*, 1998, **17**, 2313–2323.

62 G. Mund, R. J. Batchelor, R. D. Sharma, C. H. W. Jones and D. B. Leznoff, {FeCl[BuN(SiMe2)]2O}2: The first multinuclear iron(iii) complex exhibiting spin-admixture, *J. Chem. Soc. Dalt. Trans.*, 2002, 136–137.

63 V. C. Gibson, S. K. Spitzmesser, A. J. P. White and D. J. Williams, Synthesis and reactivity of 1,8-bis(imino)carbazolide complexes of iron, cobalt and manganese, *Dalt. Trans.*, 2003, 2718–2727.

64 C. Carbonera, C. A. Kilner, J.-F. Létard and M. A. Halcrow, Anion doping as a probe of cooperativity in the molecular spin-crossover compound [FeL2][BF4]2 (L = 2,6-di{pyrazol-1-yl}pyridine), *Dalt. Trans.*, 2007, 1284–1292.

65 S.-C. Liu, X.-R. Zhu, D.-Y. Liu and D.-C. Fang, DFT calculations in solution systems: solvation energy, dispersion energy and entropy, *Phys. Chem. Chem. Phys.*, 2023, **25**, 913–931.

66 J. M. Holland, J. A. McAllister, C. A. Kilner, M. Thornton-Pett, A. J. Bridgeman and M. A. Halcrow, Stereochemical effects on the spin-state transition shown by salts of [FeL2]2+ [L = 2,6-di(pyrazol-1-yl)pyridine], *J. Chem. Soc. Dalt. Trans.*, 2002, 548–554.

67 F. Neese, A critical evaluation of DFT, including time-dependent DFT, applied to bioinorganic chemistry, *JBIC J. Biol. Inorg. Chem.*, 2006, **11**, 702–711.

68 G. Schüürmann, R.-U. Ebert, J. Chen, B. Wang and R. Kühne, External Validation and Prediction Employing the Predictive Squared Correlation Coefficient — Test Set Activity Mean vs Training Set Activity Mean, *J. Chem. Inf. Model.*, 2008, **48**, 2140–2145.

View Article Online
DOI: 10.1039/D6QI00844E

69 G. Comas-Vilà and P. Salvador, Rationalizing Spin-Crossover Properties of Substituted Fe (II) Complexes, *Inorg. Chem.*, 2025, **64**, 15437–15447.

70 I. Capel Berdiell, R. Kulmaczewski and M. A. Halcrow, Iron(II) Complexes of 2,4-Dipyrazolyl-1,3,5-triazine Derivatives—The Influence of Ligand Geometry on Metal Ion Spin State, *Inorg. Chem.*, 2017, **56**, 8817–8828.

71 H. Phan, J. J. Hrudka, D. Igimbayeva, L. M. Lawson Daku and M. Shatruk, A Simple Approach for Predicting the Spin State of Homoleptic Fe(II) Tris-diimine Complexes, *J. Am. Chem. Soc.*, 2017, **139**, 6437–6447.

72 P. Comba, G. Nunn, F. Scherz and P. H. Walton, Intermediate-spin iron(iv)-oxido species with record reactivity, *Faraday Discuss.*, 2022, **234**, 232–244.

73 E. L. Onderko, M. J. Field, A. Silakov, T. H. Yosca and M. T. Green, Importance of the Ferryl Quintet State in Determining the Electronic Properties of P450 Compound I, *J. Am. Chem. Soc.*, 2025, **147**, 9147–9158.

View Article Online
DOI: 10.1039/D6QI00844E

Data for this article, including the datasets (***base_spin_dataset*** and ***T_SCO_dataset***) and the DFT optimised structures, are available at Zenodo at https://zenodo.org/records/18182735. The python codebase and GUI for Kestrel can be made available, free of charge, by emailing chem-kestrel@york.ac.uk.